# Magnetic Resonance Microscopy Analysis of Transport in a Novel Tape-Cast Porous Ceramic

**Tyler R. Brosten, Sarah L. Codd, Konstantin V. Romanenko, and Stephen W. Sofie**
Dept. of Mechanical Engineering, Montana State University, Bozeman, MT 59717

**Joseph D. Seymour**
Dept. of Chemical and Biological Engineering, Montana State University, Bozeman, MT 59717

*DOI 10.1002/aic.11872*

*Freeze-tape-cast porous ceramics allow for tailored pore structures. The impact on transport dynamics of pore structures which vary as a function of spatial depth within a ceramic is an important consideration in designing pore structures for particular applications. In this article, the application of nuclear magnetic resonance microscopy and $^1$H NMR techniques to characterize the transport in a novel tape-cast ceramic is presented.* *AIChE J*, 55: 2506–2514, 2009
*Keywords: ceramic, heterogeneous, porous media, magnetic resonance imaging, dispersion*

## Introduction

Recent advances in ceramic processing technology have introduced the ability to produce spatially evolving pore structures in which the pore dimensions exhibit one-dimensional affine characteristics.[1] These complex pore structures suggest the opportunity to design ceramics with unique transport properties for many industrial applications including fuel cells, filtration, and catalyst supports. However, the detailed nature of these pore structures including interpore connectivity has yet to be established. This experimental study utilizes established magnetic resonance microscopy and nuclear magnetic resonance (NMR) transport measurements to probe the characteristics of the freeze-tape-cast ceramic pore structure and induced transport phenomena defining this new class of ceramics with engineered porosity.

Nuclear magnetic resonance microscopy is well suited to the study of opaque porous structures because of the ability to easily obtain information concerning the dynamic behavior of a fluid or gas occupying the pore structure.[2,3] The magnetic basis of information transmission in an NMR experiment overcomes the material opacity constraint of many optically based methods historically used to study porous materials. Furthermore, NMR methods offer the ability to spatially resolve data. The spatial resolution capability is particularly attractive to this study because the ceramic samples exhibit spatial scaling of the pore structure as mentioned earlier.

The majority of reports relating to NMR-based studies of ceramic materials focus upon either solid-state type measurements[4] or image intensity-based measurements.[5–8] In parallel with these efforts, an array of NMR methodologies, e.g., gas diffusion and fluid transport techniques, have been developed which can be used to study porous materials.[2,3,9–12] These NMR techniques and others have emerged as powerful tools used in the study of structural and transport characteristics of classical porous media, e.g., monodisperse bead packs.[12–15] This article expands the application of these NMR transport techniques to the structural characterization of the novel ceramics with heterogeneous pore structures.

An overview of this article is as follows: the manufacturing process of freeze-tape-cast ceramic structures and the

---

Correspondence concerning this article should be addressed to S. L. Codd at scodd@coe.montana.edu

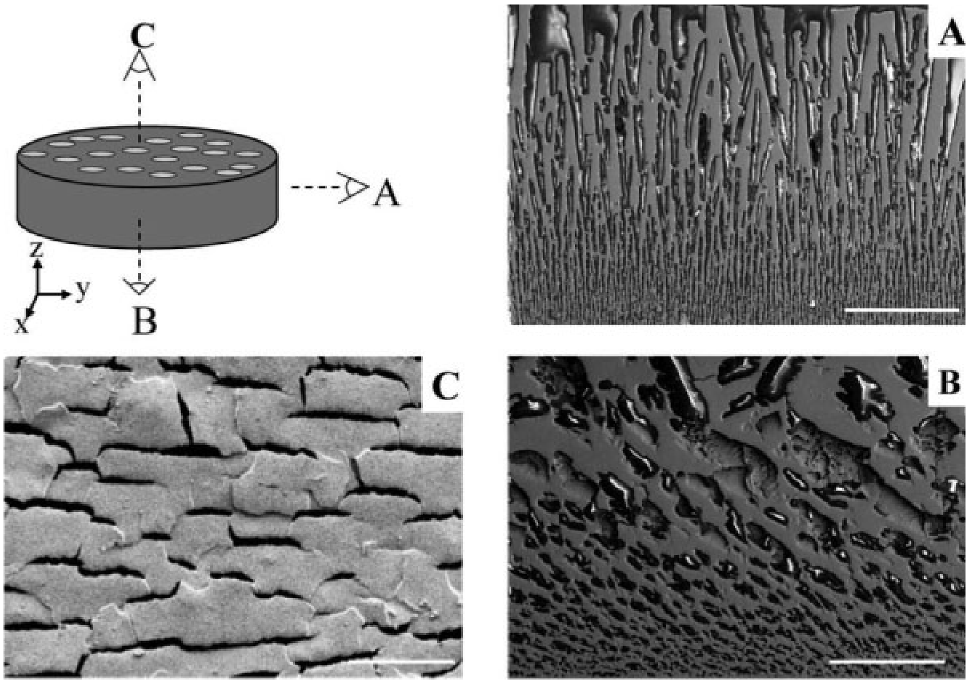

Figure 1. Typical freeze-tape-cast ceramic pore structure as viewed using SEM microscopy, bar = 400 $\mu$m.

experimental NMR methodologies used in this work is reported in the first section. The second section reports the experimental results involving a range of spatially resolved and bulk NMR measurement and the resultant analysis of the data to determine both structural pore information and transport dynamics. The third section provides concluding remarks focusing on the potential to design pore structures for controlled dynamics.

## Freeze-Tape-Cast Ceramic Pore Manufacture and Experimental Methods

The porous structures of interest in this study are manufactured using a novel freeze-tape-casting procedure.[1] The ceramic material selected is yttria-stabilized zirconium oxide (YSZ). Traditional tape-cast pore-forming techniques used in the manufacture of ceramics use homogeneously dispersed packing of thermal fugitive compounds[16] (polystyrene, carbon, etc.). The ability to control the pore structure of these traditional tape-cast ceramics is governed by the morphology of the pore former (i.e., spherical, acicular, etc.) as well as the ability to control the orientation and distribution of the thermal fugitives in a suspension, thereby limiting the precision and complexity of the pore structures that can be obtained. In addition, the drying process limits the tape thickness due to settling and drying stresses yielding cambered substrates and undesirable density gradients. Freeze casting methods have been recognized as a methodology to produce ceramic pore structures, not possible with traditional casting methods,[17–19] including graded and columnar pore morphologies in a single processing step. However, because of the complex nature of the casting dies and freezing baths, freeze casting methods are generally considered commercially unviable. The tape-casting process used in conjunction with freeze casting methods has been shown to retain the pore-forming control mechanisms of freeze casting methods while expanding the technology to commercially viable casting volumes[1]. Freeze-tape-casting yields long-range pore alignment from a controlled nucleation front allowing large area ceramic fabrication with a common pore orientation.

The SEM images of Figure 1 provide high-resolution two-dimensional pore scale detail on a limited region of the ceramic. The imaging method requires destructive sampling.

Nondestructive magnetic resonance imaging (MRI), though at lower resolution, is not limited by the opaque nature of the ceramic structure. Furthermore, dynamic MRI measurements permit the measurement of the pore structure impact on transport dynamics. Magnetic resonance imaging of pore structure is accomplished by measurement of a saturating liquid or gas spin (molecular) density $\rho(\mathbf{r})$. The resultant image is a pixel intensity map where a given pixel is weighted by the local spin density neglecting local relaxation effects. Magnetic resonance imaging methodologies are well established,[20] and only a brief description of the method is given here.

A standard two-dimensional spin-echo sequence (Figure 2) was used for spin density imaging of freeze-tape-cast ceramic pore structures.

During the acquisition period with a null applied motion sensitizing linear magnetic field gradient, $|\mathbf{g}| = 0$, the signal can be expressed as follows:

$$S(\mathbf{k}) = \int \rho(\mathbf{r}) \exp[i2\pi\mathbf{k}\cdot\mathbf{r}]d\mathbf{r}. \quad (1)$$

The two-dimensional spatial frequency vector is given by $\mathbf{k} = \gamma t(|\mathbf{g}_{\mathbf{phase}}|\hat{x} + |\mathbf{g}_{\mathbf{read}}|\hat{z})(2\pi)^{-1}$, where $\gamma$ is the gyro magnetic ratio of the signal bearing nuclei, and the phase and read encode gradients are indicated in the $\hat{\mathbf{x}}$ and $\hat{\mathbf{z}}$ unit vector

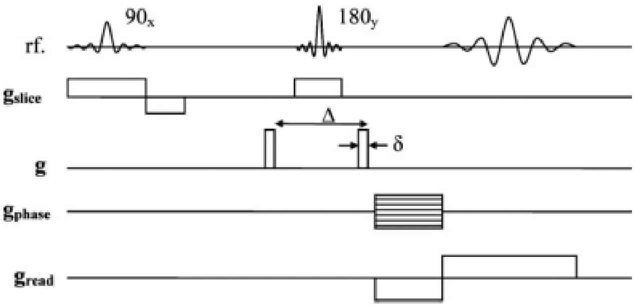

**Figure 2. Spin-echo magnetic resonance imaging radio frequency and gradient pulse sequence and a velocity phase contrasting PGSE gradient pulse pair g.**

directions. Equation 1 is a Fourier relationship and upon inverse Fourier transformation yields the two-dimensional spin density distribution $\rho(\mathbf{r})$. The bipolar pulsed field gradient pair in Figure 2, $|\mathbf{g}| \neq 0$, permits velocity weighted image contrast. As a result of nonzero values of the bipolar gradient, spins within an image voxel acquire a phase at the acquisition period due to their coherent motion over the observation time $\Delta$.[20]

$$\varphi(\mathbf{r}) = \gamma\delta\mathbf{v}(\mathbf{r})\Delta\cdot\mathbf{g}, \qquad (2)$$

where $v(\mathbf{r})\Delta$ is the average spin displacement within a voxel. A velocity map can thus be obtained from the phase difference of two images with different applied gradient values. The resultant velocity image is not a measurement of the instantaneous local average spin velocity but instead a Lagrangian measurement of velocity resulting from the average local spin displacement within a pixel over the time $\Delta$.[10] A variant of the single-pulse velocity imaging sequence of Figure 2 is the application of a second gradient pair following the first pulse pair (Figure 3), which either refocuses coherent motion over the time $\Delta$ or repeats the phase shift due to coherent motion.[20]

The signal of the refocused experiment is governed by the random dispersive movement over the observation time $2\Delta$.[21] The mixing time, $\tau$, allows for another degree of freedom in the two experiments in which spins either retain displacement correlation between the pulse pairs or decorrelate displacements for longer mixing times. In this work, $\tau$ is kept at a minimum to eliminate decorrelation over the mixing time.

The velocity phase contrast method demonstrated in Eq. 2 is a reduced form of the more generalized method of obtaining a two-dimensional image of the full displacement propagator or van Hove self-correlation function for each pixel, $P(\mathbf{R},\Delta)$.[20] The dynamic variable $P(\mathbf{R},\Delta)$ is the probability of a molecule within some averaged volume having displacement $\mathbf{R}$ over the observation time $\Delta$. The process of obtaining a two-dimensional image with full propagator resolution is time consuming. This article uses the displacement propagator from a one-dimensional spatially resolved PGSE sequence. In this sequence, the phase gradient shown in Figure 2 is removed and the signal is obtained as a function of the applied gradient magnitude. For the one-dimensional spatially resolved sequence, the signal during the acquisition period is given by

$$S(\mathbf{k},\mathbf{q}) = \iint \rho(\mathbf{r})P(\mathbf{r},\mathbf{R},\Delta)\exp[i2\pi\mathbf{k}\cdot\mathbf{r}]\exp[i2\pi\mathbf{q}\cdot\mathbf{R}]d\mathbf{r}d\mathbf{R}. \qquad (3)$$

The displacement wavelength vector is given by $\mathbf{q} = \gamma\delta\mathbf{g}(2\pi)^{-1}$. Inverse Fourier transformation of Eq. 3 yields the one-dimensional average displacement propagator $P(\mathbf{r},\mathbf{R},\Delta)$ and the one-dimensional spin density $\rho(\mathbf{r})$; the vector $\mathbf{r}$ is oriented parallel to the read direction. For a given location $\mathbf{r}$, a cumulant expansion of $P(\mathbf{R},\Delta)$ is given by the following equation[13]:

$$\log\langle e^{i4\pi^2\mathbf{q}\cdot\mathbf{R}}\rangle = \sum_{j=1}^{\infty}\frac{(i\mathbf{q})^j}{j!}X_j, \qquad (4)$$

where $X_j$ is the $j$th moment about the first moment of $P(\mathbf{R},\Delta)$. The even moments of the displacement propagator govern the signal magnitude, whereas the odd moments govern the signal phase. The velocity phase contrast method demonstrated in Eq. 2 is a first-order expression for the phase relationship given by Eq. 4 and is only valid in regions of $\mathbf{q}$ where the nonlinear odd moments are negligible. An effective dispersion coefficient is given by assuming Gaussian dynamics in which $D_{\mathrm{eff}} = \langle\sigma^2\rangle/2\Delta$; where $\sigma^2$ is the displacement distribution variance, i.e., $X_2$ in Eq. 4. With this assumption, the signal amplitude in the limit $\mathbf{q} \to 0$ of the single PGSE sequence is given by the following equation[22]:

$$S(\mathbf{r},\mathbf{q})/S(\mathbf{r},\mathbf{0}) = \exp\left(-4\pi^2|\mathbf{q}|^2\mathbf{D}_{\mathbf{eff}}(\Delta-\delta/3)\right). \qquad (5)$$

An effective diffusion coefficient over displacement time $\Delta$ for the single-pulse PGSE sequence is given by the slope of the line $\ln[S(\mathbf{r},\mathbf{q})/S(\mathbf{r},0)]$ vs. $-4\pi^2|\mathbf{q}|^2(\Delta - \delta/3)$.

All NMR experiments were conducted on a Bruker Avance DRX spectrometer system with a Bruker Micro5 probe and gradient amplifiers interfaced with a 250-MHz superconducting magnet. A custom designed sample holder was used to rigidly fix cylindrical ceramic samples within a 10-mm birdcage rf coil for the flow and diffusion measurements. The imaging was conducted on samples in a 10-mm birdcage coil. Several individual ceramic samples were used to generate the experimental data; however, all ceramic

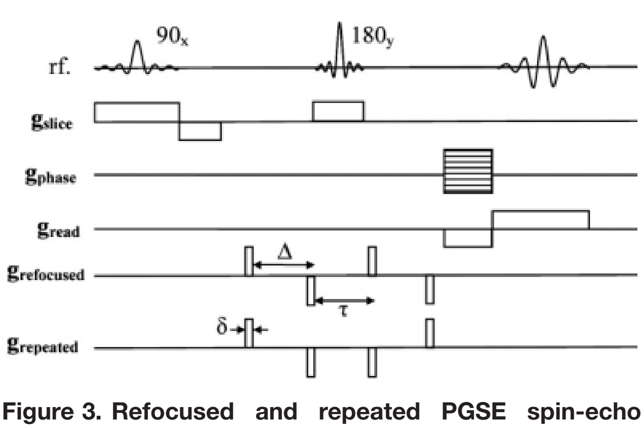

**Figure 3. Refocused and repeated PGSE spin-echo magnetic resonance imaging sequences.**

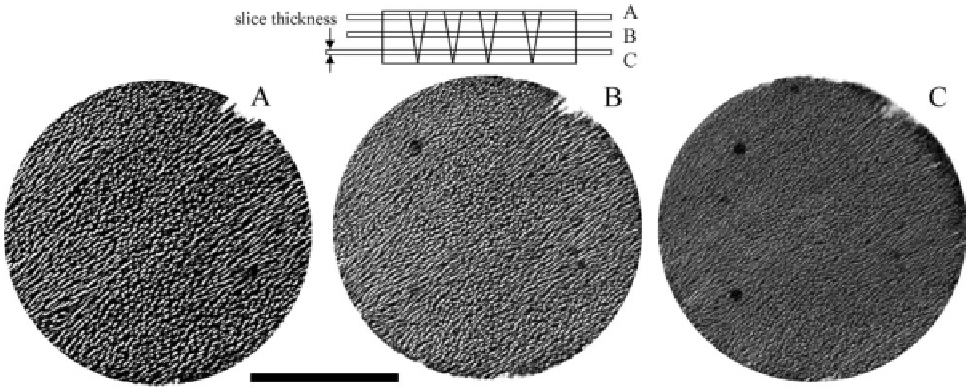

**Figure 4. Magnetic resonance imaging of a water-saturated YSZ freeze-tape-cast ceramic disk showing the transition of pore dimensions.**

Slice thickness = 200 $\mu$m, 26 × 26 $\mu$m/pixel, bar = 2.0 mm.

samples were manufactured using YSZ ceramic and an equivalent manufacturing process. The ceramic sample thicknesses varied from 1.0 to 2.5 mm. A Pharmacia P500 syringe pump created the steady laminar flow of octane through the ceramic samples. The orientation of the ceramic samples was such that the flow through the ceramic samples was always in the direction of divergent pore growth.

## Experimental Results and Discussion

### *Magnetic resonance imaging of freeze-tape-cast ceramic and PGSE diffusion probe of the pore structure*

The one-dimensional affine spatial scaling of the freeze-tape-cast ceramic pore dimensions is highly visible from magnetic resonance imaging of a Magnevist© doped water-saturated ceramic disk, as shown in Figure 4. The images shown are each a slice of 200 $\mu$m thickness from the top Figure 4A to the bottom Figure 4C of the sample. The in-plane image resolution at each depth is 26 $\mu$m × 26 $\mu$m. Note the impact of the varying pore size on the water density image. In the large pores near the upper surface (Figure 4A) regions of no signal in the ceramic and strong signal in the pores indicate that the spatial averaging scale of 26 $\mu$m is smaller than the pore size. Elongation of the pores in a preferred direction at approximately 45° to horizontal is evident. The image clearly indicates the connectivity of the pores in the image plane; information not available from SEM. As the image plane is moved into the large pore region, a blurring of the image results from the decreasing pore dimension causing partial voluming of the pore water signal and solid ceramic within the 26-$\mu$m spatial resolution.

Diffusive spin behavior has been recognized as another method to obtain pore scale information in porous media.[3] Attenuation of the PGSE NMR signal of a saturated porous media under no-flow conditions (assuming weak magnetic susceptibility-induced internal magnetic field distortions) is a result of molecular diffusion during the observation time $\Delta$. For a porous media, a comparative reduction in the nonrestricted diffusion signal attenuation occurs because at sufficient observation times, the pore structure restricts the diffusive movement of saturating molecules and therefore reduces the PGSE NMR signal attenuation.[2,3,20,21]

Using the one-dimensional spatially resolved PGSE sequence, a data set quantifying transverse restricted diffusion (perpendicular to the direction of pore growth) in a freeze-tape-cast ceramic structure was obtained by angular adjustment of a transverse gradient vector (Figure 5).

The characteristic diffusion time required for spins to sample a pore restriction is given by $a^2/D_m$, where $a$ is the characteristic pore size and $D_m$ is the molecular self-diffusion coefficient. The characteristic diffusion length scales with the square root of the observation time $l_d \propto \sqrt{D_m \Delta}$, and so smaller pores will have a larger reduction in signal attenuation when compared with larger pores because more spins will experience the pore wall restriction. Therefore, for a fixed observation time, smaller pore dimensions will result in a lower effective diffusion coefficient. Figure 6 shows the effective diffusion coefficient within a freeze-tape-cast ceramic from a single-pulse PGSE experiment with both angular and one-dimensional (parallel to pore growth direction) spatial resolution. Diffusion in the longitudinal direction over the observation time $\Delta$ coarsens the spatial resolution in the longitudinal direction. Therefore, a relatively short observation time (when compared with the expected transverse diffusive time scales of the structure) of $\Delta = 30$ ms was chosen to minimize spins longitudinal movement while allocating their dynamics to a particular longitudinal location.

The data clearly indicate depth and in-plane angular orientation of the average pore structure. Figure 6A indicates the

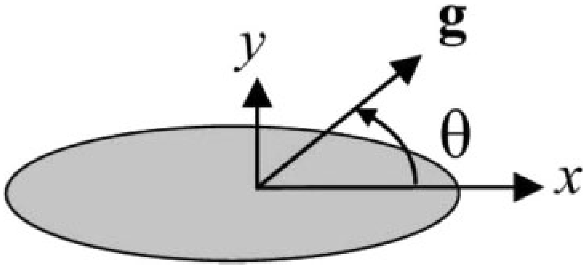

**Figure 5. Orientation of the applied gradient vector relative to the transverse pore shape for the single-pulse PGSE experiment.**

The plane shown is perpendicular to the main $B_0$ field and direction of pore growth.

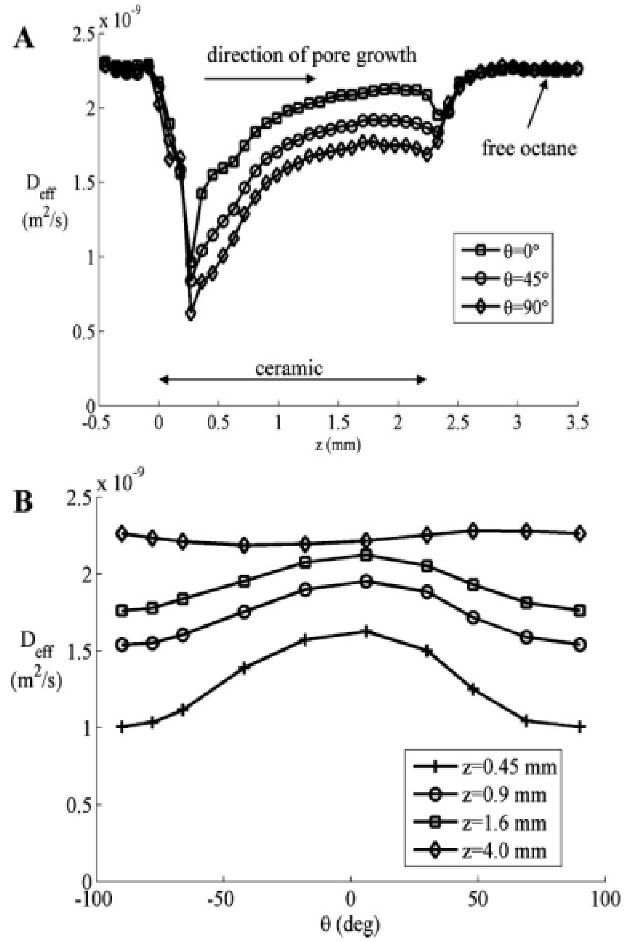

**Figure 6. Effective diffusion coefficient from the single-pulse PGSE experiment as a function of longitudinal position and transverse gradient vector, g, orientation within a YSZ freeze-tape-cast ceramic.**

$\Delta = 30$ ms, the uppermost curve of image B represents the free diffusion coefficient of octane outside of the ceramic.

growth in the average pore size from the small pore region, $z = 0$ mm, to larger pores, up to $z = 2.25$ mm. In all three in-plane orientations, there is a strong restriction of motion (small pore region) at $z = 0.25$ mm with a fairly rapid decay in the $z$-dimension until a depth of $z = 1.0$ mm, indicating a rapid increase in pore size over this region. For $z > 1.5$ mm, the effective diffusion coefficient asymptotes to in-plane orientation values below the free molecular diffusion coefficient signaling that pore growth has nearly diminished. Outside of the ceramic structure, the effective diffusion coefficient asymptotes to the room temperature self-diffusion coefficient of octane, $2.35 \times 10^{-9}$. Figure 6B shows the pore size variation with in-plane angular orientation at four depths through the variation of $D_{\text{eff}}$. The depth and angular dependence of Figure 6B is evident, and clearly a strong elongation of the pores can be seen in the three profiles within the ceramic. In the isotropic fluid outside of the ceramic, the profile is independent of the gradient orientation as seen in uppermost profile of Figure 6B. The ceramic is thus heterogeneous in both the depth and radial dimensions. This determination using NMR techniques is nondestructive and describes only the connected open-pore structure accessible by liquid penetration.

### *Spatially resolved PGSE NMR of steady pressure-driven flow through freeze-tape-cast ceramic pore structures*

Pulsed gradient spin-echo NMR techniques were used to obtain velocity weighted two-dimensional images of pressure-driven octane flowing through a freeze-tape-cast ceramic disk, shown in Figure 7. Flow direction is from the small to the large pore region by a pressure drop applied across the ceramic. The images of Figure 7 are weighted by the longitudinal component of the voxel average spin velocity vector in the $z$-axis flow direction through the disk thickness.

Figure 7A is determined through interpolation of the transverse velocity planes. From a visual interpretation of Figure 7, the velocity distribution is narrower for the small pore region. This is a result of the transverse image resolution significantly exceeding the local pore dimensions, leading to a measurement of the regional average velocity as opposed to a velocity measurement near the pore scale as seen in Figure 7B. Because of the inclined nature of the pore structure (see Figure 1B), the local enhancement of the velocity present in Figures 8B,C could indicate transitions between individual pores as the streamlines must reorient themselves upward to transition between the individual pores.

A velocity probability distribution or histogram of velocities calculated from the spatially resolved velocity images of Figure 7, represents the statistical distribution of coarse-grained velocities averaged over the voxel dimensions of the image and the observation time $\Delta$. A distribution of displacements over time $\Delta$ weighted by spin density, i.e. average propagator,[20,22] is measured using the one-dimensional spatially resolved PGSE sequence. The longitudinal spin velocity probability distribution can then be calculated by dividing the longitudinal displacement $\mathbf{R} \cdot \hat{\mathbf{z}}$ by the observation time $\Delta$. The velocity distribution of the one-dimensional spatially resolved PGSE experiment thus reflects the dynamics of spins without the spatial coarse graining inherent in the two-dimensional velocity image. Hence different spin density weighting is present in the velocity probability distribution calculated from the two-dimensional velocity images. Differences between velocity probability distributions determined from the entire spin ensemble and the spatially coarse grained images reflect the nature of the variation between the distributions of nonspatially averaged and spatially averaged dynamics.

Figure 8 shows the longitudinal velocity probability distribution from the PGSE sequence at several longitudinal positions for the steady flow of octane through a freeze-tape-cast ceramic. Overlaid on the data is the velocity distribution resulting from the spatially resolved velocity imaging sequence. The flow direction is from the small to large pore region.

In a short porous media with evolving pore structure, the concept of asymptotic dynamics is not relevant and preasymptotic dynamics or evolving dynamics must be considered. The measured velocity probabilities reflect the stationary dynamics at each depth $z$ over a displacement observation time of $\Delta = 30$ ms. At $z = 0.53$ mm, there is clear evidence of a strong peak at zero velocity and a small peak near the average velocity of 2.0 mm/s with decreasing probability of higher velocity. This behavior indicates two

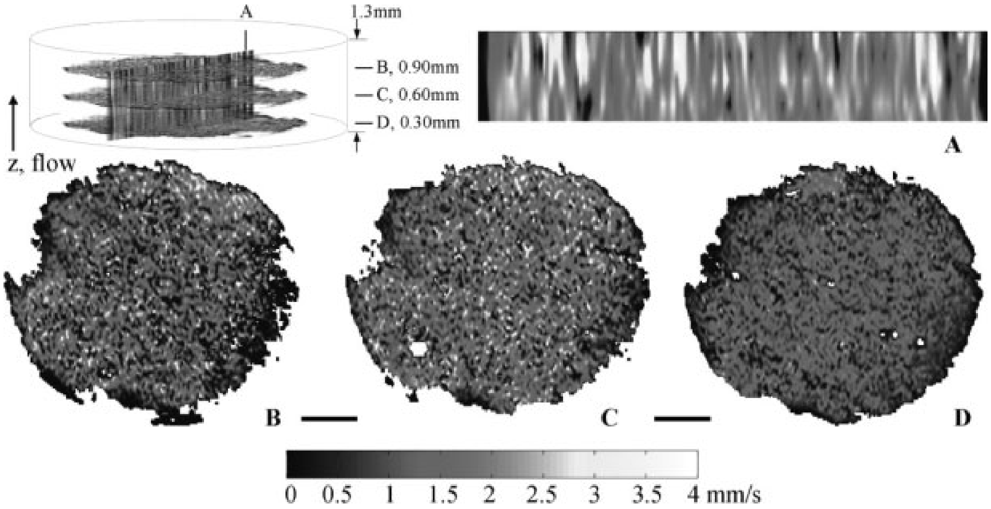

**Figure 7. Depth-resolved two-dimensional longitudinal velocity images of steady pressure-driven octane flowing through a YSZ freeze-tape-cast ceramic disk.**

Bar = 1.00 mm, 40 × 80 $\mu$m/pixel, slice thickness = 300 $\mu$m, $\Delta = 5$ ms, flow is parallel to direction of pore growth.

populations of spin dynamics, restricted and backbone, which undergo limited exchange in $\Delta = 30$ ms.[23,24] As the pore size increases with increasing $z$, at $z = 1.17$ mm depth, the propagator takes a form resembling data in model bead packs for which the displacement observation time $\Delta$ allows only a pore length displacement.[25,26] Based on the structural images, this seems to indicate spin motion within channels in which mixing is limited, i.e., dynamics are distributed continuously between spins in the low-velocity pore wall regions to the fastest spins in the pore tube center, with no mechanical or diffusive Taylor dispersion mixing in time $\Delta = 30$ ms. It should be noted that entrance effects can impact the dynamics at the upper and lower ceramic boundaries. This is indicated by a dual population of octane present downstream of the ceramic boundaries. This behavior indicates the jetting of fluid from the porous ceramic with slow flow regions between pores and a discrete volume of stagnant fluid at the outer edge of the ceramic disk. The spatial depth variation of the average porosity (fluid volume fraction) can be estimated using the two-dimensional velocity images and spatially resolved propagator data. Porosity estimations from the two-dimensional velocity images rely upon overestimation of the volumetric flow rate due to image pixel dimensions exceeding the local pore dimensions. Porosity estimations from the PGSE propagator data use the planar average fluid velocity. The average spin velocity from the single-pulse PGSE data can be calculated from the first moment of the displacement distribution,

$$\langle v_z\rangle_{xy} = \frac{1}{\Delta}\int_{-\infty}^{\infty} \mathbf{R}\cdot\hat{\mathbf{z}}P(z,\mathbf{R},\Delta)d\mathbf{R}. \tag{6}$$

The longitudinal dependence of the transverse porosity is then

$$\varepsilon_{xy} = \frac{\dot{V}_{\mathrm{act}}}{A_{\mathrm{t}}\langle v_z\rangle_{xy}}, \tag{7}$$

where $\epsilon_{xy}$ is the transverse porosity, $\dot{V}_{\mathrm{act}}$ is the known volumetric flow rate, and $A_{\mathrm{t}}$ is the total (fluid and ceramic) transverse area. The transverse area, $A_{\mathrm{t}}$ in Eq. 7, can be found using either the imaging data from Figures 7 or 4. Figure 10 shows the longitudinal distribution of the average transverse porosity estimated using the single-pulse propagator data and spatially resolved velocity images. Also shown in Figure 9 is the bulk porosity for a similar freeze-tape-cast ceramic sample estimated from an Archimedes porosity experiment.

The calculated porosity from the NMR data exhibits a minimum in porosity at the ceramic depth of 1.25 mm. The

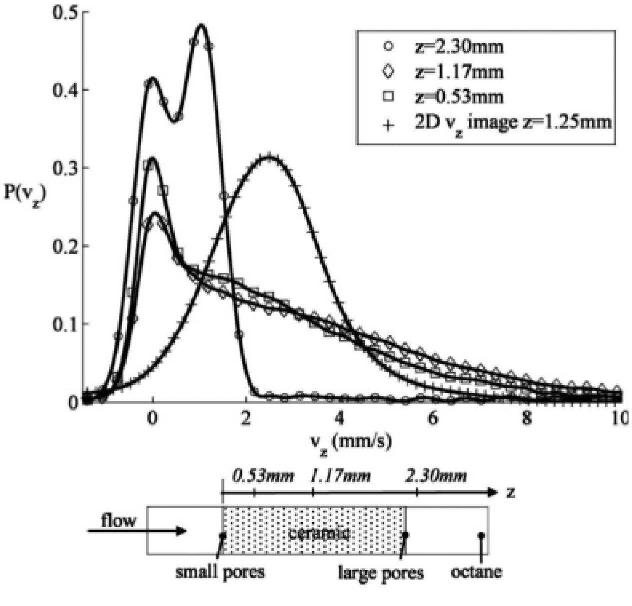

**Figure 8. Velocity probability distributions of steady pressure-driven octane from the PGSE propagator sequence for several *z*-axis locations in a YSZ freeze-tape-cast ceramic, $\Delta$ = 30 ms, flow is parallel to direction of pore growth.**

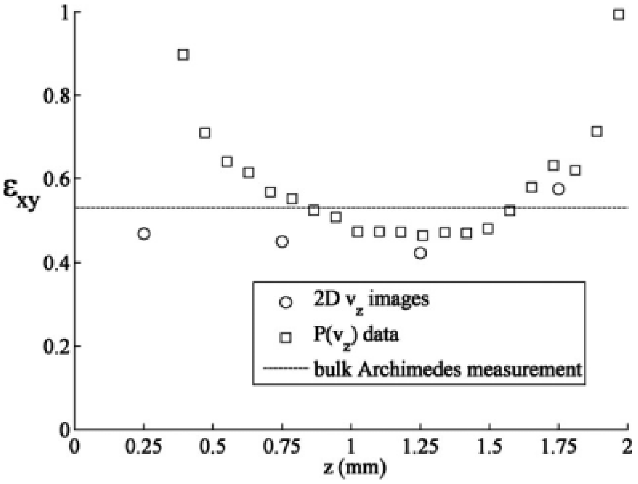

**Figure 9. Transverse porosity of a YSZ freeze-tape-cast ceramic as a function of longitudinal position from the single-pulse propagator data and spatially resolved velocity images.**

porosity calculations from $P(v_z)$ data are weighted by magnetic susceptibility effects very near the ceramic edges, i.e., ±0.5 mm, resulting in unrealistic values of the porosity.

Experiments were conducted on a freeze-tape-cast ceramic sample using the spatially resolved repeated and refocused experiments to determine the spatial dependence of the effective axial dispersion coefficient $D^*_{zz}$. Figure 10 shows the spatially resolved effective axial dispersion coefficients from the velocity-sensitive repeated PGSE and velocity-compensated PGSE pulse sequences.[27,28]

The refocused and repeated sequences vary in that the repeated sequence contains echo attenuation due to the distribution of coherent motion over the displacement time $2\Delta$ as well as diffusive or random motion. In contrast, the refocused sequence refocuses magnetization dephasing due to the spatial distribution of coherent motion and therefore echo attenuation is due to incoherent motion generated by free diffusion and mechanical dispersion only. This is achieved by reversing the effective polarity of the 2nd gradient pair in Figure 3. A comparison between Figures 10A and B indicates that the longitudinal motion of octane remains largely refocus-able for the time scale $2\Delta = 10$ ms probed. This is a consequence of the pore structure forcing the octane to maintain a relatively constant average velocity and limiting the amount of mechanical dispersion over the observation time $2\Delta = 10$ ms. Figure 7A supports the limited role of mechanical dispersion by the backbone flow behavior appearing in the image.

Using the Stejskal-Tanner approximation, the longitudinal dependence of the average axial effective dispersion coefficient was estimated from a one-dimensional single-pulse PGSE experiment, the results are shown in Figure 11. The choice of

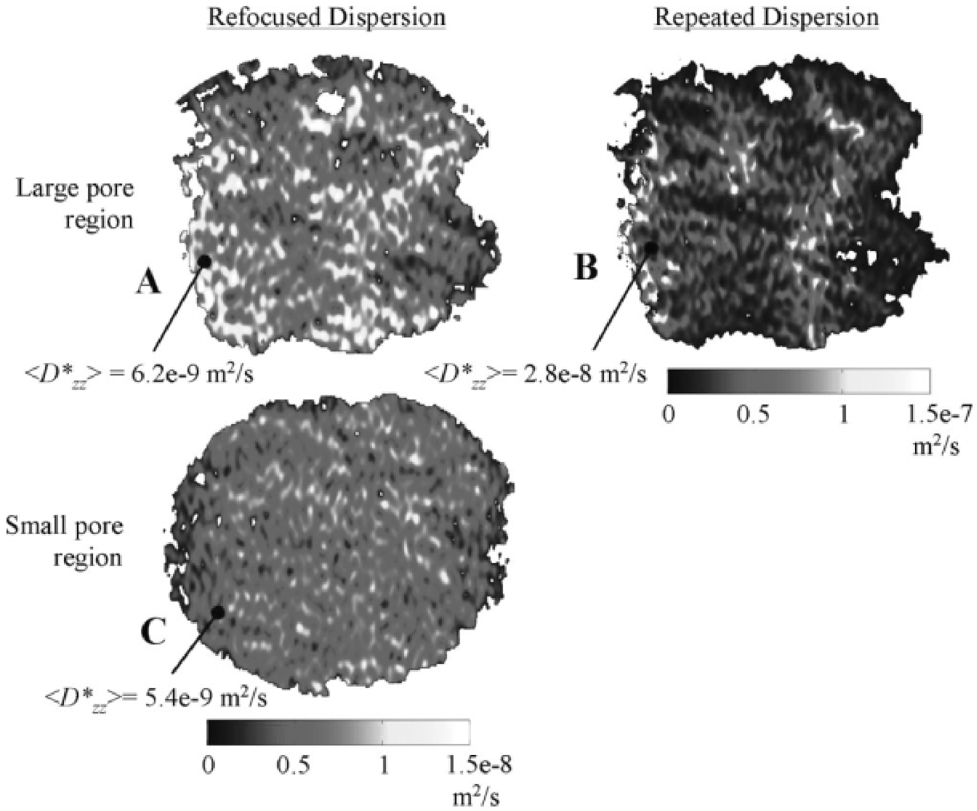

**Figure 10. Spatially resolved effective axial dispersion coefficient of steady pressure-driven octane flow in a YSZ freeze-tape-cast ceramic for the repeated and refocused echo sequences.**

80 × 160 $\mu$m/pixel, slice thickness = 300 $\mu$m, $2\Delta = 10$ ms, $\tau = 5$ ms.

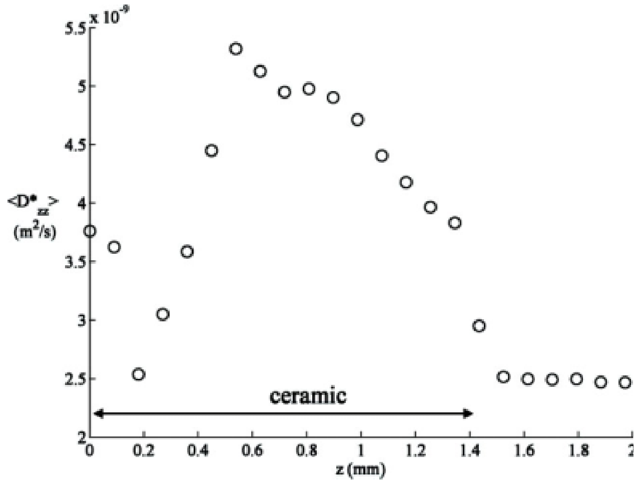

**Figure 11. Average effective axial dispersion coefficient of steady octane flow within a YSZ freeze-tape-cast ceramic, $\Delta = 30$ ms.**

observation time $\Delta$ resulted in $\Delta \ll a^2/D_\mathrm{m}$; so that the molecular diffusion-induced Taylor dispersion is small relative to mechanical and boundary layer dispersion mechanisms.

Outside of the ceramic, a measurement near the room temperature self-diffusion coefficient of octane was found. The distribution of the effective axial dispersion coefficient is a result of coupled variation in the pore dimensions and interpore connectivity. Figure 11 highlights the opportunity of these controllable pore structures to produce custom-tailored transport dynamics.

## Conclusions

A range of NMR techniques were used to characterize the pore structure of freeze-tape-cast ceramics and the pore structure impact on transport dynamics. Freeze-tape-cast ceramic pore structures prepared by a unidirectional solidification process are a complicated network of interconnected pores in which the average pore dimensions grow as a function of depth. YSZ was found to agree well with the NMR experiment constraint that the sample material should induce only weak distortions in the applied magnetic fields. Spatially resolved NMR measurements were found to provide valuable, nondestructive, and noninvasive information regarding the three-dimensional variable freeze-tape-cast pore structure. The ability to resolve both the transport and pore structure information is a valuable asset to the study of these, and other, opaque structures. Further work is needed to probe the impact of variation in freeze tape casting manufacture parameters, e.g., casting bed temperature, on the ceramic pore structure and its effect on transport dynamics. However, the data presented here outline some of the opportunities of these structures to produce unique, custom-tailored transport dynamics.

## Acknowledgments

This work was funded in part by NSF CAREER Award 0642328 to S.L.C. and an Inland Northwest Research Alliance Ph.D. Fellowship to T.R.B. The MR equipment was supported by NSF MRI CTS-0521595 and a grant from the M.J. Murdock Charitable Trust. This work was supported in part by the MSU-HiTEC program and is funded by the U.S. Department of Energy under Award No. DE-AC06-76RL01830 to S.W.S.

## Literature Cited

1. Sofie SW. Fabrication of functionally graded and aligned porosity in thin ceramic substrates with the novel freeze-tape-casting process. *J Am Ceram Soc*. 2007;90:2024–2031.
2. Callaghan PT, Coy A, Macgowan D, Packer KJ, Zelaya FO. Diffraction-like effects in NMR diffusion studies of fluids in porous solids. *Nature*. 1991;351:467–469.
3. Mitra PP, Sen PN, Schwartz LM. Short-time behavior of the diffusion-coefficient as a geometrical probe of porous-media. *Phys Rev B*. 1993;47:8565–8574.
4. Hatfield GR, Carduner KR. Solid-state NMR—applications in high-performance ceramics. *J Mater Sci*. 1989;24:4209–4219.
5. Beyea SD, Caprihan A, Clewett CFM, Glass SJ. Spatially resolved adsorption isotherms of thermally polarized perfluorinated gases in yttria-stabilized tetragonal-zirconia polycrystal ceramic materials with NMR imaging. *Appl Magn Reson*. 2002;22:175–186.
6. Beyea SD, Caprihan A, Glass SJ, DiGiovanni A. Nondestructive characterization of nanopore microstructure: spatially resolved Brunauer-Emmett-Teller isotherms using nuclear magnetic resonance imaging. *J Appl Phys*. 2003;94:935–941.
7. Hayashi K, Kawashima K, Kose K, Inouye T. NMR imaging of advanced ceramics during the slip casting process. *J Phys D: Appl Phys*. 1988;21:1037–1039.
8. Lizak MJ, Conradi MS, Fry CG. NMR imaging of gas imbibed into porous ceramic. *J Magn Reson*. 1991;95:548–557.
9. Mair RW, Wong GP, Hoffmann D, Hürlimann MD, Patz S, Schwartz LM, Walsworth RL. Probing porous media with gas diffusion NMR. *Phys Rev Lett*. 1999;83:3324–3327.
10. Seymour JD, Callaghan PT. Generalized approach to NMR analysis of flow and dispersion in porous media. *AIChE J*. 1997;43:2096–2111.
11. Stapf S, Packer KJ, Graham RG, Thovert JF, Adler PM. Spatial correlations and dispersion for fluid transport through packed glass beads studied by pulsed field-gradient NMR. *Phys Rev E*. 1998;58:6206–6221.
12. Codd SL, Altobelli SA. A PGSE study of propane gas flow through model porous bead packs. *J Magn Reson*. 2003;163:16–22.
13. Scheven UM, Sen PN. Spatial and temporal coarse graining for dispersion in randomly packed spheres. *Phys Rev Lett*. 2002;89:254501.
14. Manz B, Alexander P, Gladden LF. Correlations between dispersion and structure in porous media probed by nuclear magnetic resonance. *Phys Fluids*. 1999;11:259–267.
15. Khrapitchev AA, Callaghan PT. Reversible and irreversible dispersion in a porous medium. *Phys Fluids*. 2003;15:2649–2660.
16. Boaro M, Vohs JM, Gorte RJ. Synthesis of highly porous yttria-stabilized zirconia by tape-casting methods. *J Am Ceram Soc*. 2003;86:395–400.
17. Koch D, Andresen L, Schmedders T, Grathwohl G. Evolution of porosity by freeze casting and sintering of sol-gel derived ceramics. *J Sol–Gel Sci Technol*. 2003;26:149–152.
18. Moon JW, Hwang HJ, Awano M, Maeda K, Kanzaki S. Preparation of dense thin-film solid electrolyte on novel porous structure with parallel pore channel. *J Ceram Soc Jpn*. 2002;110:479–484.
19. Fukasawa T, Deng ZY, Ando M, Ohji T, Goto Y. Pore structure of porous ceramics synthesized from water-based slurry by freeze-dry process. *J Mater Sci*. 2001;36:2523–2527.
20. Callaghan PT. *Principles of Nuclear Magnetic Resonance Microscopy*. Oxford, England: Clarendon Press, 1991.
21. Callaghan PT, Codd SL, Seymour JD. Spatial coherence phenomena arising from translational spin motion in gradient spin echo experiments. *Concepts Magn Reson*. 1999;11:181–202.
22. Stejskal EO. Use of spin echoes in a pulsed magnetic-field gradient to study anisotropic restricted diffusion and flow. *J Chem Phys*. 1965;43:3597–3603.

23. Tallarek U, van Dusschoten D, Van As H, Bayer E, Guiochon G. Study of transport phenomena in chromatographic columns by pulsed field gradient NMR. *J Phys Chem B*. 1998;102:3486–3497.
24. Kandhai D, Hlushkou D, Hoekstra AG, Sloot PMA, Van As H, Tallarek U. Influence of stagnant zones on transient and asymptotic dispersion in macroscopically homogeneous porous media. *Phys Rev Lett*. 2002;88:234501–1–234501–4.
25. Lebon L, Leblond J, Hulin JP, Martys NS, Schwartz LM. Pulsed field gradient NMR measurements of probability distribution of displacement under flow in sphere packings. *Magn Reson Imaging*. 1996;14:989–991.
26. Maier RS, Kroll DM, Kutsovsky YE, Davis HT, Bernard RS. Simulation of flow through bead packs using the lattice Boltzmann method. *Phys Fluids*. 1998;10:60–74.
27. Caprihan A, Seymour JD. Correlation time and diffusion coefficient imaging: application to a granular flow system. *J Magn Reson*. 2000;144:96–107.
28. Seymour JD, Caprihan A, Altobelli SA, Fukushima E. Pulsed gradient spin echo nuclear magnetic resonance imaging of diffusion in granular flow. *Phys Rev Lett*. 2000;84:266–269.

*Manuscript received Nov. 19, 2008, and revision received Jan. 15, 2009.*